A reconfigurable all-fiber polarization-diversity coherent Doppler lidar: principles and numerical simulations

CYRUS F. ABARI,[1,3,*] XINZHAO CHU,[1,2] R. MICHAEL HARDESTY,[1] AND JAKOB MANN[3]

[1]*Cooperative Institute for Research in Environmental Sciences, University of Colorado, Boulder, Colorado 80309, USA*
[2]*Department of Aerospace Engineering Sciences, University of Colorado, Boulder, Colorado 80309, USA*
[3]*Department of Wind Energy, Technical University of Denmark, Roskilde DK-4000, Denmark*
Corresponding author: cyrus.abari@gmail.com

This paper shows an efficient adaptation of a polarization diversity optical front-end, commonly used in high-speed fiber-optic communications, in a coherent Doppler lidar (CDL). The adopted architecture can be employed in a modified transceiver design for an all-fiber micropulsed coherent Doppler wind lidar where the performance limits of such systems are pushed beyond the conventionally available wind CDLs. As a result, either a longer measurement range, crucial in clear-air environments with low concentration of aerosols, or a shorter integration time (resulting in a faster scanning) can be achieved. Alternatively, in certain aerosol loading conditions where the presence of nonspherical aerosols is considerable, the system can be reconfigured on the fly to analyze the cross polarization of the backscatter optical signal. The result is the capability to analyze the nature of aerosol particles for the detected range of interest. Due to full utilization of the backscatter signal, i.e., detection of co-polarization and cross polarization components, the signal-to-noise-ratio (SNR) as well as detection range is improved in this configuration. Moreover, the system is capable of providing a more reliable estimation of the aerosol backscatter coefficient when compared with the contemporary CDLs. This system employs robust and compact all-fiber subsystems, which are cost effective and widely available as off-the-shelf components.   © 2015 Optical Society of America

1. INTRODUCTION

Optical remote sensing of atmospheric parameters has been actively sought after and developed over the past few decades to provide better tools for the characterization and prediction of atmospheric and climatic phenomena. In the renewable energy industry, e.g., wind energy, remote measurement of atmospheric parameters, especially wind, is crucial for the maximization of energy production and wind turbine siting. One of the primary and highly efficient remote sensing techniques is light detection and ranging (lidar), an active measurement technique. In such instruments, a light source is employed to illuminate a target of interest, such as atmospheric molecules or aerosol particles. The backscattered light from the target is collected and analyzed to measure and quantify the parameters of interest.

Some of the first reported examples of lidars were based on a rudimentary search light technique [1] to measure the air density profiles in the upper atmosphere. In these systems, a continuous transmission of light would illuminate the targets along the beam transmission path. A scanning (receiver) telescope would collect the backscatter light from the range/altitude of interest. Later, modulation of the searchlight through a rotating mechanical shutter was suggested by Johnson *et al.* [2] resulting in measurements at longer ranges. Ever since, application of light in active instruments to measure various atmospheric parameters has grown dramatically, and the field has expanded. After the invention of the laser, a highly coherent light source became available, which enabled new measurements and pushed the boundaries of the existing ones. For instance, resonance lidars have been used to measure the temperature, wind, and densities of Fe and Na in the upper atmosphere [3,4]. Rotational Raman lidars [5] were developed to carry out remote measurements of temperature, and high spectral resolution lidars became available to provide measurements of temperature and atmospheric aerosol extinction and backscatter [6].

Among the available wind lidars, coherent Doppler lidars (CDLs) became widely popular for the measurements of wind in the troposphere [7]. CDLs measure the radial velocity of the wind by processing the wind-induced Doppler shift. The CO_2 laser was among the first adopted lasers for coherent detection of wind [8]. Due to advances in diode-laser pumping, solid-state CDLs (operating in 0.3–3 µm) became popular [8]. An eye-safe CDL operating at 2.1 µm using solid-state lasers was first reported by Henderson *et al.* [9].

Recently, all-fiber CDLs have become widely adopted for remote sensing of wind both as ground-base and airborne systems [10–12]. These systems are compact, robust, and fairly cost effective, owing to high-speed optical communication technology, which has been the driving force behind rapid improvements in fiber optic components and lasers. For instance, an airborne all-fiber continuous-wave (CW) CDL has been reported in [12] for in-flight measurement of wind and turbulence. WINDCUBE [13] from Leosphere, ZephIR [14] from ZephIR, and HALO photonics lidars [15] are commercial examples of 1.5 µm all-fiber coherent Doppler wind lidars. A modified ZephIR lidar, developed as a research instrument in collaboration with the Technical University of Denmark, is the Windscanner [16]. Compared with the commercially available ZephIR, this CW CDL has the additional capability to detect the direction of the radial velocity of wind. Recently, the systems have been retrofitted with a new optical front-end, i.e., an image-reject homodyne optical front-end [17], to improve the measurement performance.

CDLs share many principles with coherent optical communications. The majority of the available all-fiber CDLs benefits from the extensively available fiber-optic components, originally developed for fiber-optic communications. However, there seems to be a huge potential for further improvement of all-fiber CDLs if the full extent of fiber-optic communication technology, when relevant, is exploited. For instance, it was recently shown [17] that an all-fiber image-reject homodyne optical front-end, originally developed for coherent detection in optical communication, can be successfully adopted in a CW CDL. The lab results from the prototype, as the first reported all-fiber image-reject homodyne CW CDL, show significant improvement in terms of the detection velocity range as well as noise behavior. The detection improvements were significant for small values of wind speed, near-zero velocities. The improved performance results of this system were further verified through an atmospheric campaign [18]. This front architecture can be equally adopted in a long-range pulsed CDL.

In this paper, we show that a polarization diversity image-reject homodyne optical front-end, commonly employed in high-speed fiber-optic communications [19], can be adopted in a reconfigurable pulsed CDL; the lidar can be reconfigured on the fly to operate in a single or dual polarization mode depending on the atmospheric conditions detailed in the remainder of this paper. The proposed lidar in this paper has the capability to improve the performance of the contemporary all-fiber CDLs significantly. As we will show in Section 4, the reconfigurable transceiver can operate either in a high-power mode, suitable in atmospheric conditions with weak aerosol loading (resulting in weak backscatter signals) or a cross-polarization detection

mode. When in high-power mode (known as Mode II, see Section 4) two erbium-doped fiber optic amplifiers (EDFA) can operate in concert to double the average output power of the lidar; effectively, the pulse repetition rate (PRR) is doubled. To remove the possibility of interference between the transmit/receive signals, the two EDFAs are isolated by their orthogonal states of polarization. In the alternative mode (Mode I), the system has the capability to continuously monitor the depolarization of backscatter light from, e.g., nonspherical particles such as ash plumes, ice crystals, clouds, etc. To our knowledge, this is the first all-fiber CDL capable of continuous monitoring of signal depolarization from aerosol particles. Due to the nature of the coherent detection in CDLs, the depolarized portion of the backscatter signal is discarded (not detected) in the conventionally available CDLs. As a result, backscatter coefficient estimations based on the measurements performed by such CDLs is not accurate. Our proposed system, however, is capable of providing more accurate backscatter coefficient estimations because the depolarized portion of the backscatter signal is also detected.

The material in this paper is presented in a few sections. In Section 2, a mathematical model for the expected received signal power for elastic backscattering from a diffused atmospheric target is provided. Furthermore, we present the requirements for the realization of a coherent Doppler lidar system and present an example of a typical all-fiber CDL architecture. Section 3 introduces the adopted baseband signal modeling for the purposes of the performance simulations reported in this paper. In Section 4, the proposed architecture is analyzed and advantages and disadvantages are discussed. In Section 5, we show the results of our numerical simulation for the two main configurations (modes) of the proposed system in this paper. Eventually, the paper is concluded in Section 6.

2. COHERENT DOPPLER LIDAR

CDLs rely on the processing of elastic backscattering from a target (In elastic backscattering there is no transfer of energy between the light and matter. In other words, the optical wavelength of the backscatter light remains the same as the transmit light.) to extract the information of interest such as Doppler shift. In atmospheric science, the target has a diffuse nature, i.e., the mean free path between the constituents is much larger than the optical wavelength of the transmitted laser beam [20]. For maximum atmospheric penetration, the optical wavelength should be selected such that its absorption by the atmospheric constituents such as water vapor and CO_2 is minimal. Besides, eye-safety issues associated with laser transmission place harsh requirements on the transmit optical power (for a given wavelength). 1.5, 2.1, and 10 µm wavelengths (see [8,9,13,14]) have been reported for successful implementation of eye-safe CDLs attaining maximum atmospheric transmission. Despite a stronger backscatter cross section, the submicrometer wavelengths are not suitable for adoption in a CDL; high-quality diffraction-limited optics, an essential part of a CDL, is difficult to achieve for submicrometer wavelength while eye safety, probably the most important parameter in atmospheric lidars, poses stringent constraints. Wavelengths above 1.4 µm are generally considered eye safe [8]. In an

elastic-backscatter lidar, the expected backscatter energy can be expressed through the modified lidar equation [4]:

$$E_r = \eta E_t \beta(\lambda, z) T^2(\lambda, z) G(z) \frac{A}{z^2} \Delta z, \qquad (1)$$

where η is the lidar efficiency, β is the angular backscatter coefficient, T is the one-way atmospheric transmission, z is the mean distance to the measurement range, $G(z)$ is the geometric parameter for the light collection capability of the lidar at range z, A is the receiving optical antenna area, Δz is the depth of the illuminated region, and λ is the wavelength. Furthermore, E_r and E_t are the receive and transmit optical energies, respectively.

CDLs belong to a class of lidars known as diffraction-limited lidars. In diffraction-limited lidars, the amount of background light collection is minimized by restricting the field of view, i.e., the number of spatial modes seen by the lidar [21]. In CDLs, diffraction-limited operation is also a key to the existence of spatial coherence between the local oscillator and the collected backscatter signal. It can be shown [21] that, in mono-static diffraction-limited lidars, the collected signal power is maximized if the transmitter and receiver are matched to the same diffraction-limited transmit beam. In other words, the transmit and receive path should overlap in such systems, hence a coaxial system. Meanwhile, because in CDLs the phases of the return signals are compared against a reference signal, the detected signal can suffer from a small-scale Rayleigh fading (also known as target speckle noise) when backscatter is from a diffuse target (see [22] for the properties of speckle).

Equation (1) can be rewritten for a pulsed CDL to accommodate the transmit/receive geometry as well as backscatter from a diffuse target, such as atmospheric aerosols. Thus,

$$E_r = \eta E_t \beta(\lambda, z) T^2(\lambda, z) \frac{A_{\text{eff}}(z)}{z^2} \frac{c\tau}{2}, \qquad (2)$$

where τ is the pulse length, c is the speed of light in the atmosphere, and $A_{\text{eff}}(z)$ is the effective telescope area. Moreover, Eq. (2) can be expressed as

$$p_r = \eta E_t \beta(\lambda, z) T^2(\lambda, z) \frac{c A_{\text{eff}}(z)}{2z^2}, \qquad (3)$$

where p_r is the average backscatter signal power over τ time span. Following [20], it can be shown that the effective telescope area for a turbulence-free optical path is

$$A_{\text{eff}}(z) = \frac{\pi D^2}{4} \left[1 + \left(\frac{\pi D^2}{4\lambda z} \right)^2 \left(1 - \frac{z}{F} \right)^2 \right]^{-1}, \qquad (4)$$

where D is the telescope diameter and, in the event of a focused light, F is the focus distance. Furthermore, for a collimated beam ($F \rightarrow \infty$),

$$A_{\text{eff}}(z) = \frac{\pi D^2}{4} \left[1 + \left(\frac{\pi D^2}{4\lambda z} \right)^2 \right]^{-1}. \qquad (5)$$

Equation (4) is the effective telescope area in the presence of target speckle only. However, another important phenomenon in the atmosphere (atmospheric turbulence), especially for long optical paths, affects the spatial coherence of the wavefront associated with the backscatter. In the presence of atmospheric turbulence, the refractive index variations over the optical path

deteriorate the speckle. The effect of the atmospheric turbulence on the optical signal, known as scintillation, has been well investigated [21,23–26]. As a result, Eq. (4) can be modified to reflect the effect of turbulence such that

$$A_{\text{eff}}(z) = \frac{\pi D^2}{4} \left[1 + \left(\frac{\pi D^2}{4\lambda z} \right)^2 \left(1 - \frac{z}{F} \right)^2 + \frac{D^2}{2\rho_0^2} \right]^{-1}, \qquad (6)$$

where ρ_0 is the turbulence parameter (also known as "the efficiency saturation dimension" [27]) and given by

$$\rho_0 = \left[1.45 \left(\frac{2\pi}{\lambda} \right)^2 \int_0^z C_n^2(z') \left(1 - \frac{z'}{z} \right)^{\frac{5}{3}} dz' \right]^{-\frac{3}{5}}, \qquad (7)$$

where C_n^2 is known as the refractive index structure function. Typical diurnal conditions of strong and moderate turbulence can be represented by $C_n^2 = 10^{-12}$ and $C_n^2 = 10^{-14}$ [26], respectively. C_n^2 is typically largest near the ground.

It can be shown that, after some mathematical manipulation, Eq. (7) for a constant refractive turbulence level (C_n^2) reduces to

$$\rho_0 = \left[\frac{4.35}{8} \left(\frac{2\pi}{\lambda} \right)^2 C_n^2 z \right]^{-\frac{3}{5}}. \qquad (8)$$

The scintillations due to atmospheric turbulence place an upper limit on the maximum antenna area, beyond which no tangible signal-to-noise ratio (SNR) improvement is observed [25]. Contrary to the target speckle resulting from the diffuse nature of the aerosol particles, having a correlation time of a few microseconds [28], the turbulence-induced modulations (scintillations), for the applicable integration times, cannot be improved in wind CDLs by pulse averaging. For an effective improvement of the SNR degradation due to scintillations, the averaging time should be much longer than the turbulence correlation time; the turbulence correlation time is on the order of several milliseconds. As a result, a design antenna diameter can be safely selected based on the atmospheric turbulence-induced scintillation. It has been shown [25] that, in an efficient design, ρ_0 is selected as the optimum size of the receiving optics for a given range and atmospheric turbulence condition.

Figure 1 shows a simplified example of a CDL. In this system, an optical circulator (see Fig. 2) isolates the transmit and receive signals, and the collected backscatter signal, $r(t)$, is mixed with a reference signal known as the local oscillator (LO), $L_O(t)$. The mixed signal is impinged on the surface of a photodetector (PD). Coherent detection relies on spatial and temporal matching of the LO and the receive signal. The two signals should sustain a matched polarization state for a maximum detection efficiency. As a result, for an LO signal with an optical power p_{lo} and average return signal power p_r, it can be shown that the power of the detected Doppler signal, $i(t)$, at the output of the PD is [we have assumed a photodetector responsivity (detection efficiency) of unity]

$$p_i = \mathbb{E}\{|i(t)|^2\} = 2p_{lo}p_r \cos^2(\theta), \qquad (9)$$

where θ is the angle between the polarization states of LO and backscatter signals, and $\mathbb{E}\{\cdot\}$ denotes the ensemble average operation. Please note that we have dropped the z dependence of p_r in Eq. (9) for simplicity.

For an optimum performance, the LO power is selected so that the detector operates in a shot-noise limited operating
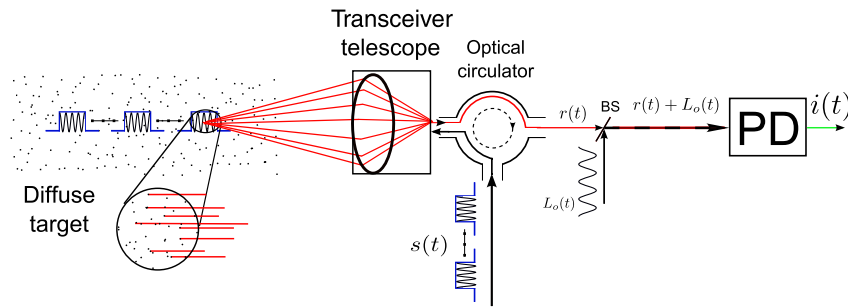
Fig. 1. Simplified illustration of a pulsed CDL. The transmitted, $s(t)$, and the local oscillator, $L_o(t)$, signals are spatially and temporary coherent. They are usually (but not necessarily) derived from a single laser known as master oscillator. BS refers to a beam splitter.
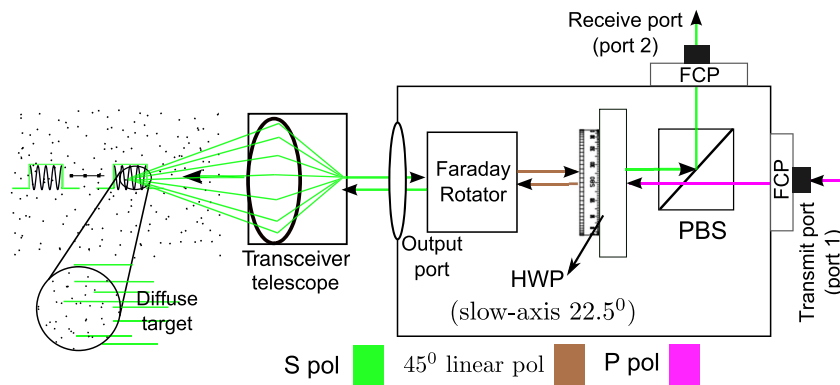

Fig. 2. Simple single polarization optical circulator. Isolation between port 1 and 2 is provided by manipulating the light polarization through the polarizing beam splitter (PBS), half-wave plate (HWP), and Faraday rotator, as shown. The fiber coupled ports (FCP) connect the optical circulator to the transmit and receiver fibers. For more information on optical circulators, please see [29,30].

mode. The shot-noise power, considered the dominant noise source, can be expressed as

$$p_{\eta_{sn}} = 2\frac{hc}{\lambda}p_{lo}B, \tag{10}$$

where B is the bandwidth (BW) of the photodetector and h is the Planck constant. Following Eqs. (9) and (10), the average SNR ($\bar{\gamma}$), for a perfect match between the polarization states of the reference and backscatter signals ($\theta = 0°$), can be defined as

$$\bar{\gamma} = \mathbb{E}\{\gamma\} = \frac{p_i}{p_{\eta_{sn}}} = \frac{p_r\lambda}{hcB}. \tag{11}$$

Equation (11) shows the high sensitivity of coherent detection; this system reaches an SNR = 0 dB per unit BW for each single photon.

The ensemble average in Eq. (11) is a reminder for the random nature of the backscatter power resulting from the speckle. The instantaneous SNR, γ, associated with the return from one single pulse, has an exponential distribution and can be expressed as [28]

$$p_\gamma(\gamma) = \frac{1}{\bar{\gamma}}\exp\left(-\frac{1}{\bar{\gamma}}\gamma\right), \tag{12}$$

where $p_\gamma(\gamma)$ is the probability distribution function (PDF) of γ.

3. ALL-FIBER SINGLE-POLARIZATION CDL AND BASEBAND SIGNAL MODELING

Before recent advances in fiber-optic technology, CDLs relied on bulky open-space optics for the generation, transmission, and manipulation of the optical signals. CO_2 and diode-pumped Tm:Lu:YAG laser CDLs [8] are examples of such systems. With the revolutionary advances in fiber-optic technology, a wide variety of fiber-optic components became available. Examples of such components are fiber-optic lasers, amplifiers, beam couplers, etc. These components are compact, robust, and cost-effective, when compared with their open-space counterparts. Due to their minimum transmission loss at 1.5 μm, optical fibers have become the dominant means of optical information transmission at 1.5 μm.

A 1.5 μm wavelength also happens to belong to an optical spectral region with a maximum atmospheric transmission. As a result, all-fiber lidars have become the dominant players in the CDL market, e.g., see [13,15] for instances of commercially available all-fiber long-range (pulsed) CDLs. In such systems, fiber lasers (or fiber-coupled semiconductor lasers) with a linewidth better than 5 kHz are available. Besides, the availability of EDFAs has provided a linear low-noise alternative for optical signal amplification in these systems. Because the majority of EDFAs exhibit μJ optical powers in the pulsed amplification mode, pulsed all-fiber CDLs are also known as micropulsed

CDLs. The PRR, however, is relatively high in EDFAs (on the order of several kilohertz), thus making the average output power comparable with some of the more high-energy pulsed open-space technologies such as the ones discussed in [8]. Despite a relatively comparable average power, the performance of the two types of systems is not necessarily equivalent (A comparative analysis of the two systems is beyond the scope of this paper and the interested reader can consult [31] for further information.) Among other things, the dominant factors in CDLs are the attainable pulse peak power and the system's ability to suppress the target speckle through pulse averaging. Thus, the performance of the system is determined by an intricate interplay between the pulse energy and the number of pulse averaging.

Figure 3 shows an example of an all-fiber CDL in master oscillator power amplifier (MOPA) configuration. In this figure, the master optical source is a narrow linewidth fiber coupled CW laser with an average optical output of tens of milliwatts. The pulse shaper (modulator) can be a mechanical chopper, an acousto-optic modulator (AOM), or an electro-optic modulator (EOM). The signal train at the output of the modulator is fed into an EDFA for amplification. The result passes through the optical circulator and, after proper beam expansion and focusing (or collimation), is transmitted through the atmosphere. As the pulse travels through the atmosphere, it illuminates the atmospheric constituents, e.g., aerosols. The backscatter from the particles is collected by the telescope and passed through the circulator until it reaches the balanced mixer. A detailed description of a balanced mixer, employed in a continuous wave (CW) CDL, has been provided in [17]. The LO and receive signal $r(t)$ are mixed by a 50% fiber-optic coupler and impinged on a pair of balanced PDs. The resultant current at the output of each balanced PD is further amplified and conditioned for digitization. After digitization, the two signal components are combined appropriately, and the Doppler spectrum of the return signal is processed to extract the parameters of interest, e.g., the wind velocity.

The pulse modulator in the system shown in Fig. 3 is usually an AOM. The main benefit of AOM in such systems is a simultaneous modulation of amplitude and frequency while providing a high extinction ratio between on and off states.
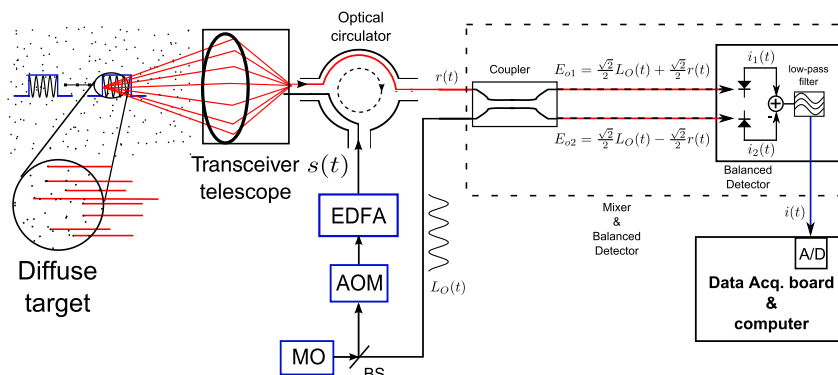
As a result of a frequency offset at the intermediate frequency (IF), the sign of the detected Doppler shifts can be discriminated. This is at the cost of a reduced BW efficiency associated with the PDs and the analo-to-digital converters (A/D). It has been shown in [17] that, by employing an all-fiber image-reject homodyne optical front-end, made originally available to the high-speed optical-communication industry, the signals can be translated into baseband where the requirement for an IF offset is eliminated. Although the optical front-end in [17] is adopted for a CW CDL, it can be easily employed in a pulsed CDL. Figure 4 shows the schematic of a single-polarization all-fiber image-reject homodyne long-range (pulsed) CDL.

To provide a better understanding of the detected signals at the output of the PD associated with the system in Fig. 4, the complex baseband mathematical signal model introduced by Rye [32] can be readily adopted in this system. In this model, the scattering amplitude of the particles is assumed to be time-invariant unless affected by a Doppler shift. If the compressed transmit pulse associated with the system in Fig. 4 is $s(t)$, then the Doppler-free baseband signal can be expressed as

$$i(t) = k \int_0^{+\infty} s(t - t') \sum_{l=1}^{N} \alpha_l \delta(t' - t_l) \mathrm{d}t', \quad \textbf{(13)}$$

where α_l, denoting a time-invariant scattering amplitude of the lth particle, is a complex-valued random variable (RV) with independent real and imaginary components having a Gaussian distribution and t_l is the time shift associated with the lth particle. Furthermore, N is the number of scattering particles and k is a constant scaling factor representing any optical attenuation, transceiver efficiency, photodetector responsivity, etc., not shown in Eq. (13).

Equation (13) reflects the diffuse nature of the target. The above equation also can be expressed as a convolution such that

$$i(t) = s(t) \otimes h(t), \quad \textbf{(14)}$$

where $\otimes$ is the convolution operator and $h(t) = k \sum_{l=1}^{N} \alpha_l \delta(t - t_l)$ represents the channel response function, a terminology commonly used in wireless communications. Equation (13) does not reflect the Doppler effect and, as a result, needs to be modified so that the motion of the particles is included. Thus [32]
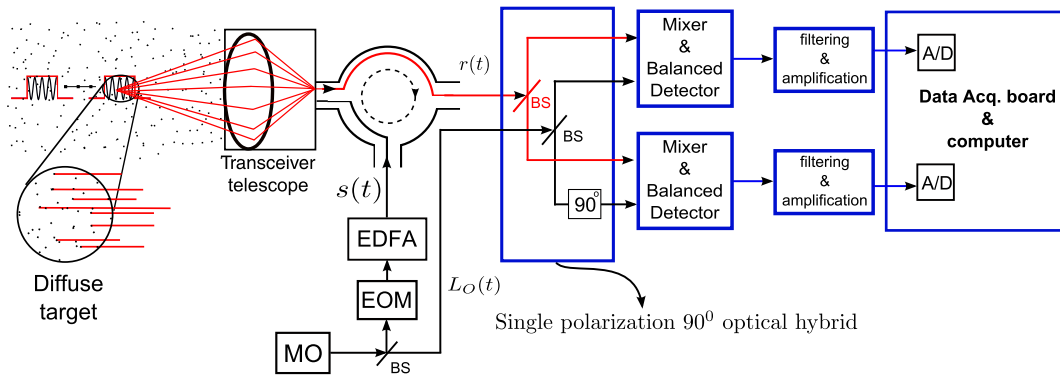

Fig. 3. Single-polarization heterodyne pulsed CDL with IF sampling. The AOM is responsible for chopping the signal received from the MO and generating the required optical pulses while shifting the transmit signal frequency to an IF offset. The balanced mixer and detector utilized the full power of the collected backscatter signal while removing the DC and any common mode components from the L_O and $r(t)$ signals [17].

Fig. 4. Single polarization image-reject homodyne pulsed CDL. In this system, the pulse generator can be an EOM, which does not introduce any frequency offset in the transmit signal. The image-reject homodyne receiver translates the Doppler signal into baseband for further processing. The image-reject homodyne receiver, also known as direct-conversion receiver, eliminates the need for an IF offset (enabling the detection of Doppler signal sign).

$$i(t) = k \iint_0 s(t - t') \exp[j2\pi f'(t - t')]$$
$$\times \sum_{l=1}^{N} \alpha_l \delta(t' - t_l)\delta(f' - f_l)\mathrm{d}t'\mathrm{d}f', \qquad (15)$$

where $s(t - t') \exp[j2\pi f'(t - t')]$ is the frequency-shifted pulsed waveform, f_l is the frequency shift associated with the lth particle, and j is the imaginary unit. Equation (15) is associated with the detected signal over the entire measurement range. Considering the fact that the pulse illuminates different sets of particles as it propagates through the atmosphere the return signal decorrelates. As a result, a shorter sample volume where a certain spatial correlation between the scattering particles, hence the scattered light, exists needs to be used for the Doppler shift estimation. We can expect the range gate to completely decorrelate once the pulse has traveled a distance equivalent to the pulse length.

In light of the above discussion, Eq. (15) needs to be truncated for each range gate of interest. Range gating also allows the estimation of the Doppler spectra for specific ranges over the maximum measurement range. Thus, if $w(t - t_0)$ is the window function with a width equivalent to the length of the range gate (t_0 is the center of the range gate), then

$$i_T(t) = w(t - t_0)i(t). \qquad (16)$$

Following [32], and, after some mathematical manipulations and simplifications, it can be shown that

$$P_{i_T}(f) = \mathbb{E}\{|I_T(f)|^2\}$$
$$= k^2 \sum_{l=1}^{N_0} \mathbb{E}\{|\alpha_l|^2\}[|W(f)|^2$$
$$\otimes |G(f)|^2 \otimes \mathbb{E}\{P_{T_0}(f)\}], \qquad (17)$$

where $P_{i_T}(f)$ is the power spectral density (PSD) of $i_T(t)$, while $I_T(f)$, $W(f)$, and $G(f)$ are the continuous time Fourier transforms (CTFT) of the truncated signal, window, and pulse, respectively. Furthermore,

$$P_{T_0}(f) = \sum_{l=1}^{N_0} \delta(f - f_l) \qquad (18)$$

is the Doppler spread function associated with the (N_0) particles belonging to the range gate centered at t_0. It is evident from Eq. (17) that the Doppler spectrum of the detected signal is the convolution of the pulse and window function PSDs, and the Doppler spectrum associated with the particles in the sampling volume.

4. ALL-FIBER POLARIZATION DIVERSITY IMAGE-REJECT COHERENT DOPPLER LIDAR

As seen from Eq. (9), the detection efficiency is maximized if the LO and backscatter signals retain the same polarization state. As a result, in the majority of all-fiber CDLs, polarization-maintaining (PM) fibers are used for the transmission and manipulation of light. The only exception is a CW CDL where the LO is taken from the end facet of the delivery fiber by Fresnel reflection [10]. In this case, the LO and backscatter signal follow the same path in the system and experience the same polarization variations. In such a system, single mode (SM) fibers can be conveniently used in place of PM fibers. A detailed description of such a system architecture can be found in [10,17]. Due to system design requirements, where the LO and backscatter signal (after collection by the telescope) experience different paths before mixing at the receiver, the long-range (pulsed) CDLs need to employ PM fibers to guarantee maximum overlap between the polarization states of the receive and LO signals.

In this paper, we suggest a new all-fiber optical front architecture where an image-reject homodyne receiver such as the one in [17] is used for the translation of Doppler information into the baseband. Furthermore, we suggest a polarization diversity optical front-end, conventionally used in high-speed fiber-optic communications [19], to take advantage of the additional degree of freedom provided with an extra polarization state of light. In other words, we suggest the system operates on the basis of two orthogonal polarization states. The orthogonality of the polarization states helps us to separate the

two signals without any noticeable interference. The system is designed such that it is capable of detecting the depolarized signal component, if any. Backscatter light depolarization is a common phenomenon when probing aerosols with non-spherical shapes; for instance, (ash) clouds and ice crystals are examples of natural atmospheric phenomena where non-spherical particles may constitute a significant part of the aerosols. In the event of clear air atmosphere, with a relatively low amount of light depolarization, the system can double its average output power by interleaving the transmit pulsed with orthogonal polarization states while maintaining its range.

Figure 5 shows the schematic of such a system. As we can see, an MO is used to generate narrow linewidth CW radiation. The optical power is usually in the range of tens of milliWatts. For the system configuration in Fig. 5, the state of polarization of the laser light at the output of the MO can be 45°. A beam splitter (BS) allows a small amount of the power to be diverted as LO signal. The signal at the output of the BS, right after MO, is fed into the first polarizing beam splitter (PBS). The PBS receives the laser (having a polarization of 45°) and divides it in half, where two orthogonal polarization states, i.e., p- and s-polarization states are separated at the output legs. The optical switch on the s-polarization leg allows the system to operate in two configurations. When the switch is on, the system operates with maximum output power. In other words, it allows two separate pulse trains to be transmitted simultaneously without interfering with each other; the two pulse trains are isolated in polarization. We call this operating Mode II. If the switch is off, i.e., Mode I, then the system operates with only one polarization, p polarization. This operation mode is suitable in measurement in atmospheric conditions where nonspherical particles are expected. For instance, if the laser pulse propagates through clouds, a certain degree of depolarization can be observed [33].

A. Mode I (for the Detection of Depolarized Signals)

In Mode I, the system operates with only one EDFA. Due to a limited single-mode fiber core size (employing single-mode fibers), such EDFAs are usually average power limited. Hence, one may increase the pulse energy by decreasing the PRR; most EDFAs operate within certain PRR and pulse energy limits before nonlinearities and other unwanted spurious effects kick in. Besides, increasing pulse energy at the cost of PRR reduces the effective number of pulse averaging at the receiver for a given integration time. A detailed discussion of EDFAs and their limitation is well beyond the scope of this report.

Because the optical switch is turned off (when operating in Mode I), only the pulses from the p-polarization leg are transmitted through the polarization diversity optical circulator and eventually the telescope. The optical circulator essentially isolates the transmit and receiver signals and should ideally eliminate the cross talk between its three ports. Due to nonideal behavior of the components used to build the optical circulator, there is always a certain degree of cross talk between the ports. Imperfections in beam alignment also can be troublesome. The polarization diversity optical circulator is more complex than the single-polarization optical circulator. The architecture proposed by Roth *et al.* [34] can be adopted for a polarization diversity circulator. As soon as the pulse starts propagating through the atmosphere, the backscatter signal is collected and continuously recorded (the signal associated with the range of interest is isolated through range gating, a processing done later at the receiver) and passed to PBS 3. At the output of PBS 3, the signal is divided into two components with orthogonal polarization states, i.e., p and s. (In this paper, co-polarization and cross-polarization backscatter signals are defined with respect to the polarization state of the transmit signal. The portions of the backscatter signal having polarization states parallel and orthogonal to the transmit signal's polarization state are
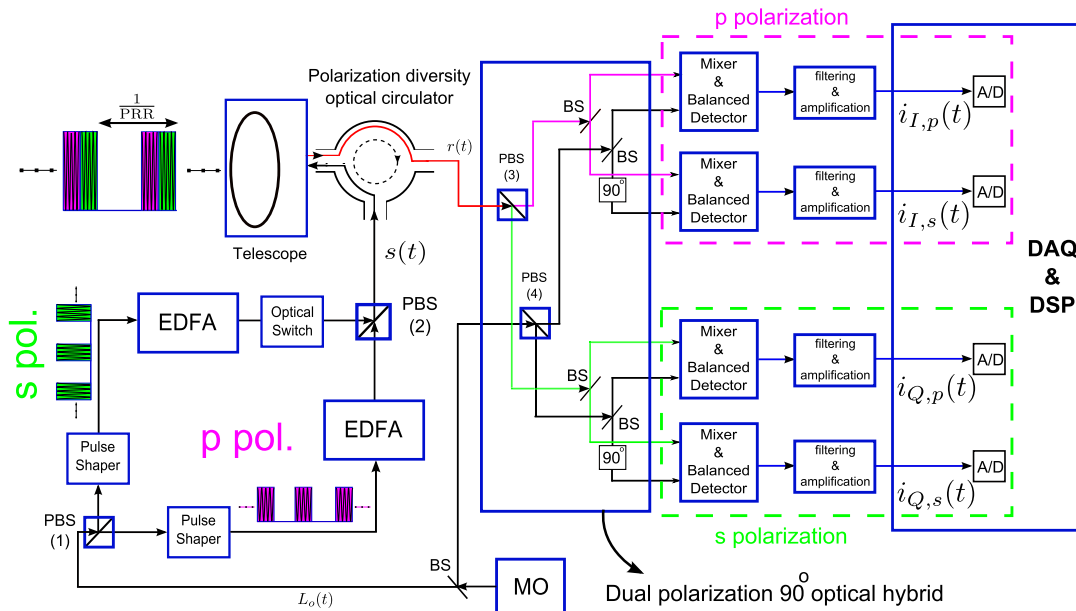

Fig. 5. Reconfigurable polarization-diversity image-reject homodyne pulsed CDL presented in this paper. The dual-polarization 90° optical hybrid [19] is responsible for splitting the receive signal into its orthogonal polarization components while providing the necessary phase shifts for the translation of the Doppler signals into baseband.

identified as co-polarization and cross-polarization signals, respectively.) If atmospheric depolarization is negligible, then the backscatter signal retains its polarization state, and the signal is present on only one leg at the output of PBS 3. The polarization state of the received light depends on the optical circulator design and technology. If a polarization-diversity optical circulator is employed in the system, the return signal will exhibit the cross polarization when compared with the originally transmitted signal. In this specific case, where p pol is transmitted, s pol (identified with the green colored signal paths in Fig. 5) is received at the input of PBS 3. If there is any tangible backscatter depolarization, the cross polarization (in this case, p polarization) will be detected by the upper detection chain (pink optical path) while the s polarization (green optical path) is detected by the lower detection chain in Fig. 5. The ratio between the two detected signals can provide some information about the nature of the aerosol particles. As a result, one benefit from the additional information provided by this CDL is to characterize the aerosols associated with different range gates.

The possibility of detecting the depolarized signals, as opposed to dumping them (a method conventionally used in single-polarization CDLs), also improves the SNR in this system. The system effectively collects all the available backscatter signals (including the depolarized signal) within its field of view for detection at the PDs. In such a system, a maximum ratio combining (MRC) technique (e.g., see [35]) commonly used in wireless communications can be used to maximize the SNR for any given signal strength on the two polarization states. This system is also able to improve the SNR degradation seen in single-polarization CDLs from nonideal optical components and surfaces (such as mirrors) that contribute to a certain amount of signal depolarization. Moreover, it is expected that the two backscatter light components (with orthogonal polarization states) experience different speckle patterns. This can be expected due to the nonspherical nature of the particles. As a result, the SNR is further improved due to an additional degree of speckle diversity in this configuration. In a single-polarization pulsed lidar, pulse averaging for each range gate helps to improve the SNR. This is due to the physical nature of the (target) speckle; target speckle has a correlation time of a few microseconds. As much as a twofold speckle diversity improvement (in the event of signal depolarization) can be expected in this configuration; the spectra from the two polarization channels are processed separately and combined in a MRC fashion before being fed to the ML estimator.

B. Mode II (for Operation in Clear Air)

This mode is particularly beneficial in measurement scenarios where the aerosol concentration is low in the measurement volume; a requirement for this mode is that the aerosols are mostly spherical, so the amount of backscatter light depolarization is minimal. In the event of backscatter signal depolarization, the cross-polarization component of the backscatter signal associated with one pulse train will interfere with the backscatter from the other, resulting in range ambiguity at the receiver; this is due to the fact that the pulses with orthogonal polarization are interleaved, as explained later in this section. As a result, this mode can be safely used after an initial scan of the measurement

volumes (in Mode I) has been performed. If no significant depolarization is observed, the system can be switched into Mode II. To take into account the variations in atmospheric conditions and aerosol types, a certain measurement and scanning scheme can be developed where the system switches between Mode I and II periodically to account for possible depolarization at certain range gates during the measurement time. Another main merit of this system is improving the measurement speed by reducing the required integration time for a given measurement accuracy. This is especially useful in scanning or airborne CDLs.

If the optical switch is on, then the two pulse trains are interleaved at the output of PBS 3. One of the design parameters in this system is the interleaving pattern. By controlling the timing (delay) between the p and s polarization pulses, generated by the pulse modulators and synchronized by a master driver/controller, one can decide where the pulses are placed relative to each other. For instance, the interleaved pulses can be placed in equal distances from each other. Although this seems an obvious choice for the given pulse trains, it may cause interference with the collected backscatter signal at the optical circulator. This is mainly attributed to the possible leakage and nonideal behavior of the optical circulator; due to a cross talk in the optical circulator as well as back reflections from the telescope, high-energy optical pulses will leak back to the PDs (on both polarization legs) while leaving the telescope. This is one of the main reasons why the pulsed lidars are incapable of measuring the short ranges immediately after the output of the telescope. This range is proportional to the pulse length; the longer the pulse, the longer the blind detection range, i.e., the blind spot.

To address the above-mentioned issue, we suggest placing the interleaved pulses immediately next to each other. As a result, we prevent detector saturation during the measurement of a specific range, which coincides with the timing of the alternate polarized pulse transmission. The downside is that the blind spot size doubles. This system mode, however, is mostly used for the measurement of longer ranges so the deterioration of the short-range measurement capability (blind zone) may not be significant. The added benefit of placing the alternate polarized pulses next to each other is maximizing the correlation between the backscatter signal associated with each polarization state. Atmospheric correlation time is on the order of a few microseconds [28]. Any backscatter signal for a specific range gate decorrelates between the transmission of consequent pulses [32] (in a single-polarization CDL) probing the measurement range. To our knowledge, the pulse repetition rate at its highest (available in all-fiber CDLs) is on the order of tens of kilohertz. Thus, the pulse separation in time is on the order of milliseconds. As a result, no correlation between the backscatter signals associated with two consecutive pulses is expected. In our proposed interleaved pulse scheme, the two pulses with orthogonal polarization states travel together, separated only by the polarization and a time interval equivalent to the pulse length (typical pulse length in such systems is on the order of 200–400 ns). Thus, the backscatter signals associated with a pair of traveling pulses for each measurement range are expected to be correlated.
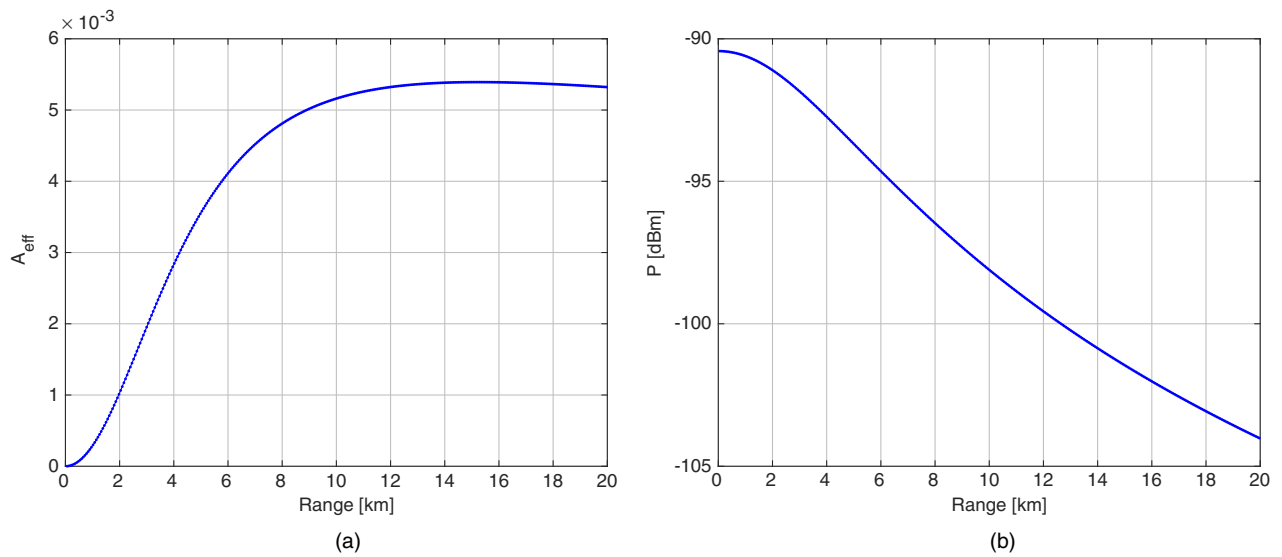
Fig. 6. Effective telescope area and expected return signal power associated with one channel for the parameters in Table 1. (a) The effective telescope area. (b) The Mie backscatter signal power.

5. SIMULATION RESULTS

To characterize the performance of the system presented in this paper, we have carried out a Monte Carlo simulation of the lidar system in MATLAB. The simulation of the lidar return can be carried out in a number of ways [32]. We have adopted the spectral-synthesis method, originally introduced by Zrnic [36] for radar. This method has been reliably used to simulate lidar return in literature (e.g., see [32]) and is computationally fast. Because a thorough performance analysis of the system, covering the nonideal behavior of the components, is beyond the scope of the current paper, we have assumed ideal CDL behavior; the detectors have a responsivity of unity, the optical circulator does not exhibit any leakage or cross talk, and the only noise source is the shot noise of the PD, which is assumed to be spectrally flat (white Gaussian noise).

We have adopted Eq. (3) for the atmospheric simulation, where the atmospheric transmission is affected by both aerosol and molecular backscatter. Because the Mie backscatter coefficient is unpredictable for different ranges and altitudes, we have assumed a uniform scattering of identical particles in the air; Mie extinction (α_{Mie}) and backscattering (β_{Mie}) coefficients have assumed to be equal in magnitude where $\alpha_{\mathrm{Mie}} = \beta_{\mathrm{Mie}} = 1.8 \times 10^{-7}$ m^{-1}. The simulations have been performed for a lidar located at an altitude of 1 km from sea level with a horizontal beam (horizontal scan) measuring in one single direction. To estimate the contribution of Rayleigh scattering, we have used the well-known molecular volume and angular

scattering equations for a given atmospheric temperature and pressure, e.g., see [4], in combination with the U.S. Standard Atmospheric model [37]. Figure 6(a) shows the effective telescope area for a collimated beam while Fig. 6(b) depicts the average Mie backscatter power for different ranges. For spectral processing, we have adopted the Periodogram [38] associated with each range gate where zero padding has been applied to smooth out the spectrum. Please note that zero padding does not provide any extra information and has a curve fitting effect on the processed spectra. To estimate the mean Doppler shift, a maximum likelihood estimator (ML) was employed. The ML
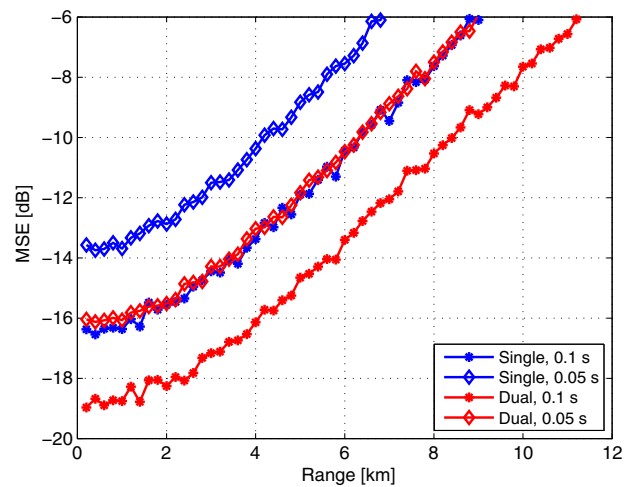

Fig. 7. Mean square error (MSE) of the mean wind speed estimator versus range. Single channel represents the MSE for one polarization state. Dual channel represents the MSE when the data from both polarization channels is utilized (combined). The values are estimated for two different integration times, i.e., 0.1 and 0.05 s. The upper −6 dB limit corresponds to a mean radial wind speed estimation error (standard deviation) of 0.5 m/s.

Table 1.　System Simulation Parameters

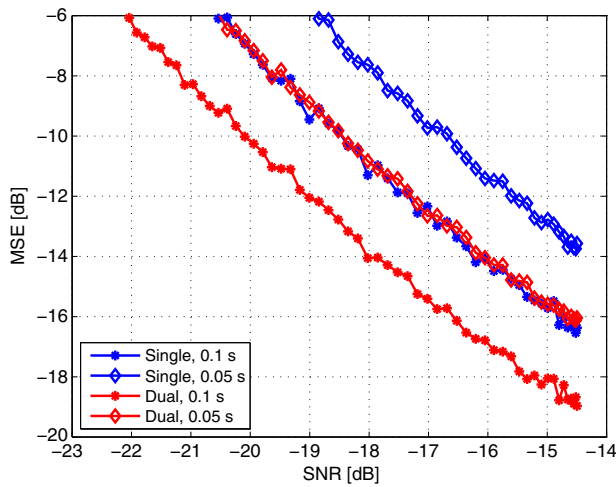| E_t [μJ]	110	PRR [kHz]	20
BW [MHz]	100	f_s [MHz]	100
Pulse length [ns]	300	range gate [m]	90
Integration time [s]	0.1, 0.05	N	512
D [cm]	10	C_n^2	10^{-14}

Fig. 8.   MSE of the mean wind speed estimator versus SNR. Single channel represents the MSE for one polarization state. Dual channel represents the MSE when the data from both polarization channels is utilized (combined). The values are estimated for two different integration times, i.e., 0.1 and 0.05 s. An upper limit of –6 dB corresponds to an estimation error (standard deviation) of 0.5 m/s.

performance can reach the Cramer–Rao lower bound (CRLB) [39]; the CRLB is the lower achievable bound on the variance of any estimator. Furthermore, a relatively narrowband Doppler spectrum [39], normalized variance of 0.02, was chosen for the simulations. A detailed list of simulation parameters is given in Table 1.

Figure 7 shows the mean square error (MSE) of the mean wind speed estimator associated with Mode II. The "Single" legend in the graph refers to the spectra acquired from only one channel, i.e., only one polarization state. The "Dual" refers to the scenario where the spectra from both channels (both polarization states) are averaged. Furthermore, the simulations have been carried out for two different integration times. It is

evident from this figure that the effect of employing a dual polarization configuration where two EDFAs operate in concert (as described in Section 4) is a consistent improvement of 3 dB in MSE (1.5 dB in standard deviation) across different ranges. Please note that in this simulation we have ignored the range beyond which the MSE is above –6 dB; a mean speed estimation deviation of 0.5 m/s is equivalent to a –6 dB in estimator MSE. Another observation from Fig. 7 can be made. The MSE associated with the dual polarization configuration with an integration time of 0.05 s is consistent with the MSE for a single polarization mode with an integration time of 0.1 s. A factor of 2 reduction in the integration time for the dual polarization mode is attractive when operating the CDLs. We know from experience that one of the problems associated with a scanning CDL is the long time intervals associated with carrying out a full scan. By employing a dual polarization CDL, the scanning time in most wind CDLs can be improved by a factor of 2. Figure 8 shows the MSE versus SNR (per channel) and is a more objective way to assess the performance when compared with the plots in Fig. 7.

To illustrate the performance of the system in Mode I, we have assumed a depolarization of 30%. As we have described in Section 4, the system operates with only one EDFA in this mode while detecting in co-polarization and cross-polarization components from the depolarized backscatter signal. The main benefit of this configuration is providing more information about the nature of the aerosol particles for each range gate. The added benefit is an improvement in the detected SNR, which results in an improved estimated mean speed. Figure 9(a) shows the MSE for the estimated mean speed calculated for a number of ranges. The simulation has been performed for an integration time of 0.05 s and a maximum MSE of –6 dB (0.5 m/s in standard deviation of mean wind speed estimator). As we can see from Fig. 9(b), an SNR improvement of 1 dB is observed when the cross polarization is combined with the co-polarization signal using an MRC technique in the spectral domain.
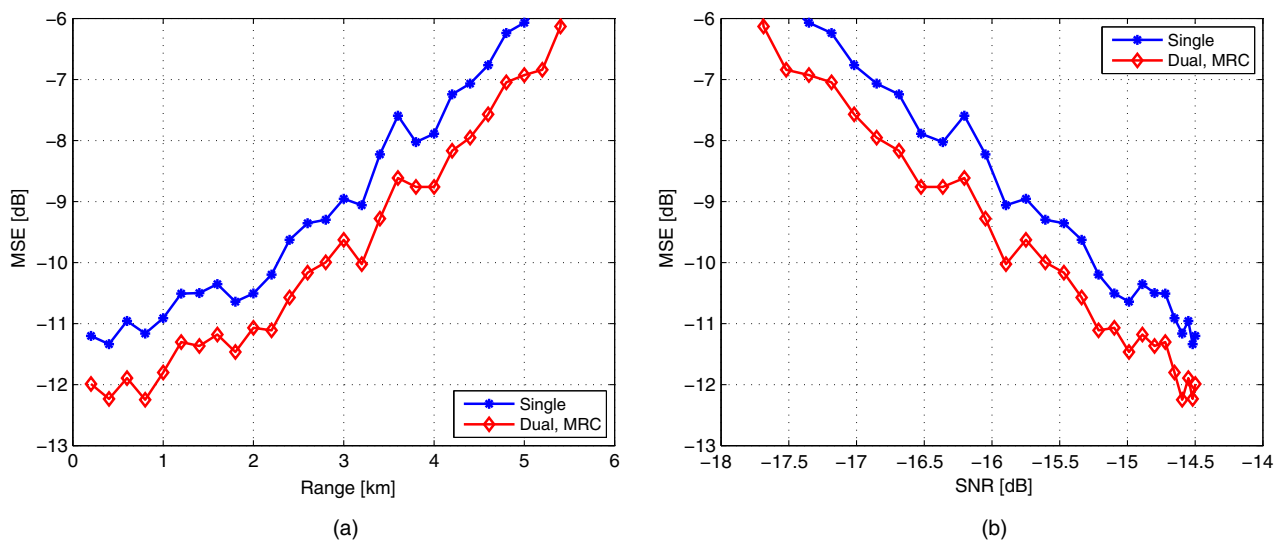

(a)

(b)

Fig. 9.   MSE of the mean wind speed estimator associated with operation Mode I. The simulations have been done following the relevant parameters given in Table 1. A 0.05 s integration time and signal depolarization of 30% have been selected in this simulation. (a) MSE versus range. (b) MSE versus SNR.

6. CONCLUSIONS

All-fiber CDLs can benefit from the more mature and advanced optical communication technology. The adoption of relevant technologies in fiber-optic communications allows us to push the performance of the all-fiber CDLs. In this paper, we showed that, by employing an all-fiber polarization-diversity image-reject optical front-end, not only faster-scanning and longer-range systems can be developed for the measurement of wind speed but also a simultaneous measurement of signal depolarization can be carried out, where relevant. The detection of the depolarized signal can provide information about the nature of the aerosols for different ranges. This system is capable of providing more reliable estimation of the backscatter coefficient, which is due to the ability of the system to detect the polarized and depolarized portions of the backscatter signal. Another merit of this system is its application in airborne deployments. Due to the aircraft's high speed, the integration time for each range is expected to be limited. As a result, doubling the PRR while maintaining the pulse energy allows for improved mean wind speed estimations in such systems. This system has the flexibility to be reconfigured on the fly to operate in two different modes. Due to its flexibility, it can be adopted in any coherent detection system, and its application is not limited to remote sensing of wind.

REFERENCES

1. E. O. Hulburt, "Observations of a searchlight beam to an altitude of 28 kilometers," Appl. Opt. **27**, 377–382 (1937).
2. E. A. Johnson, R. C. Meyer, R. E. Hopkins, and W. H. Mock, "The measurement of light scattered by the upper atmosphere from a search-light beam," Appl. Opt. **29**, 512–517 (1939).
3. X. Chu, W. Pan, G. C. Papen, C. S. Gardner, and J. A. Gelbwachs, "Fe Boltzmann temperature lidar: design, error analysis, and initial results at the North and South Poles," Appl. Opt. **41**, 4400–4410 (2002).
4. X. Chu and G. Papen, "Resonance fluorescence lidar for measurements of the middle and upper atmosphere," in *Laser Remote Sensing*, T. Fujii and T. Fukuchi, eds., (CRC Press, 2005), pp. 179–432.
5. Y. F. Arshinov, S. M. Bobrovnikov, V. E. Zuev, and V. M. Mitev, "Atmospheric temperature measurements using a pure rotational Raman lidar," Appl. Opt. **22**, 2984–2990 (1983).
6. P. Piironen and E. W. Eloranta, "Demonstration of a high-spectral-resolution lidar based on an iodine absorption filter," Appl. Opt. **19**, 234–236 (1994).
7. R. T. Menzies and R. M. Hardesty, "Coherent Doppler lidar for measurements of wind fields," Proc. IEEE **77**, 449–462 (1989).
8. R. M. Huffaker and R. M. Hardesty, "Remote sensing of atmospheric wind velocities using solid-state and CO_2 coherent laser systems," Proc. IEEE **84**, 181–204 (1996).
9. S. W. Henderson, C. P. Hale, J. R. Magee, M. J. Kavaya, and A. V. Huffaker, "Eye-safe coherent laser radar system at 2.1 μm using Tm, Ho:YAG lasers," Appl. Opt. **16**, 773–775 (1991).
10. C. J. Karlsson, F. Olsson, D. Letalick, and M. Harris, "All-fiber multi-function continuous-wave coherent laser radar at 1.55 m for range, speed, vibration, and wind measurements," Appl. Opt. **39**, 3716–3726 (2000).
11. G. N. Pearson, P. J. Roberts, J. R. Eacock, and M. Harris, "Analysis of the performance of a coherent pulsed fiber lidar for aerosol backscatter applications," Appl. Opt. **41**, 6442–6450 (2002).
12. S. M. Spuler, D. Richter, M. P. Spowart, and K. Rieken, "Optical fiber-based laser remote sensor for airborne measurement of wind velocity and turbulence," Appl. Opt. **50**, 842–851 (2011).
13. "WINDCUBE V2, a 200 m vertical wind Doppler lidar," http://www.leosphere.com/products/vertical-profiling/windcube-v2, 2015.
14. "ZephIR 300 technical specifications," http://www.zephirlidar.com/resources/technical-specs, 2015.
15. "Halo photonics pulsed Doppler LiDAR," http://halo-photonics.com, 2015.
16. T. Mikkelsen, J. Mann, M. Courtney, and M. Sjöholm, "Lidar-based research and innovation at DTU wind energy–a review," J. Phys. **524**, 012007 (2014).
17. C. F. Abari, A. T. Pedersen, and J. Mann, "An all-fiber image-reject homodyne coherent Doppler wind lidar," Opt. Express **22**, 25880–25894 (2014).
18. C. F. Abari, A. T. Pedersen, E. Dellwik, and J. Mann, "Performance evaluation of an all-fiber image-reject homodyne coherent Doppler wind lidar," Atmos. Meas. Tech. **8**, 4145–4153 (2015).
19. "COH28 dual-polarization 90° optical hybrid," http://kylia.com/?portfolio=90-hybrid-coh, 2015.
20. C. M. Sonnenschein and F. A. Horrigan, "Signal-to-noise relationships for coaxial systems that heterodyne backscatter from the atmosphere," Appl. Opt. **10**, 1600–1604 (1971).
21. S. F. Clifford and L. Lading, "Monostatic diffraction-limited lidars: the impact of optical refractive turbulence," Appl. Opt. **22**, 1696–1701 (1983).
22. J. W. Goodman, "Some fundamental properties of speckle," J. Opt. Soc. Am. **66**, 1145–1150 (1976).
23. D. L. Fried, "Optical heterodyne detection of an atmospherically distorted signal wave front," Proc. IEEE **55**, 57–77 (1967).
24. R. Frehlich, "Effects of refractive turbulence on coherent laser radar," Appl. Opt. **32**, 2122–2139 (1993).
25. I. Goldstein, P. A. Miles, and A. Chabot, "Heterodyne measurements of light propagation through atmospheric turbulence," Proc. IEEE **53**, 1172–1180 (1965).
26. A. Belmonte and B. J. Rye, "Heterodyne lidar returns in the turbulent atmosphere: performance evaluation of simulated systems," Appl. Opt. **39**, 2401–2411 (2000).
27. A. Dabas, P. H. Flamant, and P. Salamitou, "Characterization of pulsed coherent Doppler LIDAR with the speckle effect," Appl. Opt. **33**, 6524–6532 (1994).
28. A. Belmonte, "Statistical model for fading return signals in coherent lidars," Appl. Opt. **49**, 6737–6748 (2010).
29. T. Matsumoto and K. Sato, "Polarization-independent optical circulator: an experiment," Appl. Opt. **19**, 108–112 (1980).
30. M. Koga and T. Matsumoto, "High-isolation polarization-insensitive optical circulator for advanced optical communication systems," J. Lightwave Technol. **10**, 1210–1217 (1992).
31. R. Frehlich and M. J. Yadlowsky, "Performance of mean frequency estimators for Doppler radar and lidar," J. Atmos. Oceanic Technol. **11**, 1217–1230 (1994).
32. B. Rye, "Spectral correlation of atmospheric lidar returns with range-dependent backscatter," Appl. Opt. **7**, 2199–2207 (1990).
33. H. Cho, P. Yang, G. W. Kattawar, S. L. Nasiri, Y. Hu, P. Minnis, C. Trepte, and D. Winker, "Depolarization ratio and attenuated back-scatter for nine cloud types: analyses based on collocated CALIPSO lidar and MODIS measurements," Opt. Express **16**, 3931–3948 (2008).
34. J. M. Roth, R. E. Bland, and S. I. Libby, "Large-aperture wide field of view optical circulators," IEEE Photon. Technol. Lett. **17**, 2128–2130 (2005).
35. H. T. Hui, "The performance of the maximum ratio combining method in correlated Rician-fading channels for antenna-diversity signal combining," IEEE Trans. Antennas Propag. **53**, 958–964 (2005).
36. D. S. Zrnic, "Simulation of weatherlike Doppler spectra and signals," J. Appl. Meteor. **14**, 619–620 (1975).
37. *U.S. Standard Atmosphere* (U.S. Government Printing Office, 1976).
38. M. H. Hayes, *Statistical Digital Signal Processing and Modeling* (Wiley, 1996), pp. 391–424.
39. B. J. Rye and R. M. Hardesty, "Discrete spectral peak estimation in incoherent backscatter heterodyne lidar. I: spectral accumulation and the Cramer-Rao lower bound," IEEE Trans. Geosci. Remote Sens. **31**, 16–27 (1993).